Ion acceleration at two collisionless shocks in a multicomponent plasma

Rajesh Kumar[1], Youichi Sakawa,[2,*] Takayoshi Sano[2], Leonard N. K. Döhl[3], Nigel Woolsey[3], and Alessio Morace[2]

[1]*Graduate School of Science, Osaka University, Toyonaka, Osaka 560-0043, Japan*
[2]*Institute of Laser Engineering, Osaka University, Suita, Osaka 565-0871, Japan*
[3]*York Plasma Institute, Department of Physics, University of York, Heslington, York YO10-5DD, United Kingdom*

Intense laser-plasma interactions are an essential tool for the laboratory study of ion acceleration at a collisionless shock. With two-dimensional particle-in-cell calculations of a multicomponent plasma we observe two electrostatic collisionless shocks at two distinct longitudinal positions when driven with a linearly polarized laser at normalized laser vector potential a_0 that exceeds 10. Moreover, these shocks, associated with protons and carbon ions, show a power-law dependence on a_0 and accelerate ions to different velocities in an expanding upstream with higher flux than in a single-component hydrogen or carbon plasma. This results from an electrostatic ion two-stream instability caused by differences in the charge-to-mass ratio of different ions. Particle acceleration in collisionless shocks in multicomponent plasma are ubiquitous in space and astrophysics, and these calculations identify the possibility for studying these complex processes in the laboratory.

I. INTRODUCTION

Collisionless shocks under ambient magnetic field are ubiquitous in space and astrophysical plasmas and are believed to be sources for high-energy particles or cosmic-rays [1–7]. Multiple collisionless shocks occur in plasmas associated with planetary systems [8–10], where multicomponent plasmas occur as planetary material mixes with the solar wind. In the magnetospheres of planets, such as Mars and Venus, see Bertucci *et al.* [11], multicomponent plasmas occur and ions of differing charge-to-mass ratio likely play a role. Jarvinen *et al.* [12] discuss the role of oxygen in an induced Martian magnetosphere, where oxygen is likely introduced by the past solar wind bombardment of water on the unmagnetized surface of Mars. Multiple-reflection of solar-wind protons at the Martian bow-shock was recorded across a shock by Mars Express and described by Yamauchi *et al.* [13]. These observations and the Voyager missions, see for example Gurnett *et al.* [14], show multiple collisionless shocks are associated with planetary and stellar systems. Borisov and Fraenz [15] illustrates this for Mars and Venus where the formation of a second collisionless shock, in a region of magnetic pile-up between the bow shock and ionosphere [16], results from the presence of planetary oxygen ions and solar wind protons.

Collisionless shocks occur in much more extreme astrophysical systems [17–19] such as supernova remnants where a reverse shock, an inward-propagating collisionless shock, heats stellar ejecta material containing a mixture of protons and heavy ions [17]. Warren *et al.* [17] observe localized regions where strong line emission of Fe and Si ions occur in the reverse-shock heated ejecta. Yamaguchi *et al.* [20] illustrate collisionless electron heating at the front of the reverse shock caused by a cross-shock potential created by charge deflec-

tion. Understanding of collisionless shocks and the associated particle acceleration processes in multicomponent plasmas is of general importance in space, astrophysics, and plasma physics.

While multiple collisionless shocks are expected in such systems, it is not possible to observe them because of the limited resolution of the remote sensing. It is possible that future spatially resolved measurements using multipoint spacecraft clusters might observe double-shock structures. Cohen *et al.* [21] and Broll *et al.* [22] demonstrate *in situ* spatially resolved proton reflections [21] and multi-ion (solar wind protons and He^{2+} contamination) reflections [22] from a shock in the Earth's magnetosphere with the magnetospheric multiscale (MMS) cluster. Laboratory experiments are a unique way of obtaining spatially resolved measurements of collisionless shocks. They can provide tests of understanding of particle acceleration in multiple collisionless shocks. Numerical simulations by Schaeffer *et al.* [23] demonstrate the formation of two collisionless shocks as a laser-ablated plasma acts as a piston pushes on a magnetized multicomponent CH plasma. Laboratory studies show how ion separation in unmagnetized multicomponent plasma is a common occurrence [24–28]. As examples, Byvank *et al.* [24] use merging plasma jets at oblique angles to observe ion and shock-front separation when using jets that contain a mixture of He and Ar. Rinderknecht *et al.* [28] observe ion velocity separation in a laser-driven collisional shock generated in a multicomponent plasma, and ion-species separation is predicted in inertial confinement fusion experiments as a strong shock enters the fuel containing multiple-ion species [26,27].

Continuing advances in high-intensity laser technology [29] drives the development of compact, high-flux sources of energetic ions [30,31]. These sources may prove useful for many applications [32–34]. Among the many ion acceleration mechanisms being pursued [35–46], collisionless shock acceleration (CSA) of ions [47–59] is of particular relevance

---

*sakawa-y@ile.osaka-u.ac.jp

to space and astrophysical shocks. With CSA, ions located ahead of an unmagnetized electrostatic (and collisionless) shock [7] are reflected by the electrostatic potential of the shock to twice the shock velocity [49].

Unmagnetized electrostatic collisionless shocks [60,61] are rare among space [62] and astrophysical systems since shocks occur in collisionless magnetized plasma. However, there are common and important collisionless processes involved in both type of shocks [48]. For example, particle acceleration occurs in collisionless shocks [63,64], reflected particles excite two-stream instabilities [65,66], reflected ions cause shock dissipation and reformation [62,66,67], effects of cross-shock electrostatic potential [21,68], and so on. Bale *et al.* [69] describe shock dissipation due to ion reflection in terms of the Cluster satellite mission. Therefore, understanding of collisionless shocks and the associated particle acceleration processes in multicomponent plasmas is of general importance in space and astrophysical shocks. The study of collisionless shocks and particle interaction is possible with laser-plasma systems. In this work the collisionless shock is mediated by an electrostatic interaction.

In laser-plasma experiments hydrogen and carbon are ever-present on the surfaces of solid targets and inevitably result in multicomponent plasmas. A number of studies [53,54,56,58] specifically use multicomponent thin-foil targets such as plastic (CH) or Mylar ($C_{10}H_8O_4$), and in Kumar *et al.* [59] we reported on how target composition influences CSA by comparing C_2H_3Cl, CH, He^3H, and H. Inclusion of a high-atomic-number element like Cl results in partial ionization to Cl^{15+}, enabling the study of a material with $\langle Z \rangle / \langle A \rangle < 0.5$. An electrostatic ion two-stream instability (EITI) excited in the multicomponent plasma is central to the ion acceleration process with CSA accelerating protons [59] and heavier ions to the same velocity.

In comparison, the radiation pressure acceleration studies by Zhang *et al.* [70], which use circularly polarized laser pulses and a three-layer "sandwich" target containing protons and heavier ions, show the emergence of two shock fronts. One shock is associated with protons and the other with heavier ions, the different species of ion are accelerated in different fields to different velocities.

In this paper we examine, using the two-dimensional (2D) particle-in-cell (PIC) simulation code EPOCH [71], the physical conditions for the appearance of collisionless shocks and ion acceleration in a multicomponent plasma formed from C_2H_3Cl and CH targets. We use a linearly p-polarized laser pulse, and for a normalized vector potential $a_0 \geqslant 10$, to show the existence of two collisionless shock fronts. These shocks are associated with the proton and C^{6+} ion populations. The shock front accompanying the proton population propagates faster than the shock accompanying the C^{6+} ions. As a result, CSA of protons and C^{6+} ions occurs at different shocks and longitudinal locations in the plasma, producing ion populations at different velocities.

II. PARTICLE-IN-CELL SIMULATION

We study four values: $a_0 = 3.35$, 10, 20, and 33, where $a_0 = 3.35$ corresponds to 1.4×10^{19} W/cm^2 for the wavelength of 1 μm. The simulated laser pulse uses a Gaussian
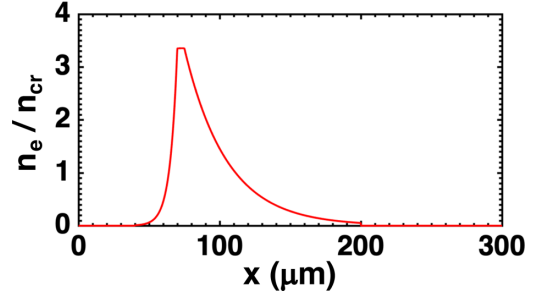

FIG. 1. The normalized initial electron density profile used in PIC simulations for $a_0 = 3.35$. The laser is from the left-hand side of the simulation box. The density profile consists of an exponentially increasing 5 μm scale-length laser-irradiated front region, followed by 5 μm uniform central region, and an exponentially decreasing rear-side profile with 30 μm scale length. To avoid boundary effects, the simulations use 40 and 100 μm vacuum regions at the front and rear of the target, respectively.

temporal profile with 1.5 ps full-width-at-half-maximum. Figure 1 shows the normalized initial electron density profile used in PIC simulations for $a_0 = 3.35$. The simulated targets use a longitudinal (*x* direction in Figs. 2 to 5) density profile consisting of an exponentially increasing 5 μm scale-length laser-irradiated front region, 5 μm uniform central region, and an exponentially decreasing profile with 30 μm scale-length rear region as the back of the target. Details of the simulations including the target density profiles at $a_0 = 3.35$ are given in Kumar *et al.* [59]. When a_0 is varied, the maximum electron density is increased to match the relativistic critical density $a_0 n_{cr}$, where $n_{cr} = 1.12 \times 10^{21}$ cm^{-3} is the critical plasma density to the laser at 1 μm. The charge states Z_i of protons, C ions, and Cl ions are 1, 6, and 15, respectively. The corresponding ion density for each material is calculated from the quasineutral plasma condition.

At $a_0 = 3.35$, as the relativistic electrons move through the plasma, the inertia of the more massive ions sets up an electrostatic field E_x. The exponentially decreasing density profile on the rear side of the target results in an electrostatic field or target-normal-sheath-acceleration field, E_{TNSA} [59]. This TNSA field occurs in the upstream region and results in the upstream ions moving at velocity v_0 in the longitudinal direction [72].

To accelerate the ions via the CSA mechanism, the potential energy at the collisionless shock must exceed the kinetic energy of the upstream expanding ions. In other words, the electrostatic potential ϕ at the shock front satisfies the following condition [73]: $Z_i e\phi \geqslant \frac{1}{2} A_i m_p (V_{sh}^i - v_0^i)^2$, where e is the electric charge, A_i is the ion mass number, m_p is the proton mass, V_{sh}^i is the shock velocity, and the superscript i represents the different ion species. The lower ion-velocity threshold v_L^i for ion reflection and CSA is $v_L^i = V_{sh}^i - \sqrt{2(Z_i/A_i)e\phi/m_p}$ [59]. Therefore, CSA occurs for

$$v_L^i \leqslant v_0^i \leqslant V_{sh}^i. \tag{1}$$

Equation (1) represents the lower v_L^i and upper V_{sh}^i bounds in v_0^i for ion reflection. All ions with velocities v_0^i between v_L^i and V_{sh}^i are reflected at the collisionless shock and leave with velocity $2V_{sh}^i - v_0^i$ and the maximum velocity is
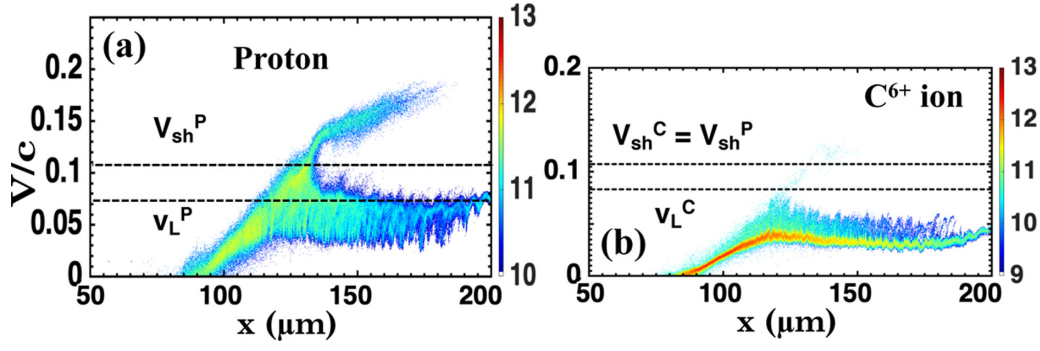
FIG. 2. Phase-space of (a) protons and (b) C^{6+} ions for C_2H_3Cl plasma at $a_0 = 3.35$ and at $t = 4.0$ ps. The horizontal lines represent the lower threshold v_L^i for ion reflection and the shock velocity in proton density V_{sh}^P. The color scale shows the number of ions in a log scale.

$V_{sh}^i + \sqrt{2(Z_i/A_i)e\phi/m_p} = 2V_{sh}^i - v_L^i$. For protons $Z_i = A_i = 1$, and the lower threshold is $v_L^P = V_{sh}^P - \sqrt{2e\phi/m_p}$.

III. RESULTS

A. Double-shock formation

Figure 2 shows the phase-space of protons and C^{6+} ions at $a_0 = 3.35$. A significant population of protons satisfy Eq. (1) and as result are accelerated at the collisionless shock [Fig. 2(a)]. In comparison, relatively few C^{6+} ions are reflected by the same collisionless shock, as this requires $V_{sh}^C = V_{sh}^P$ [Fig. 2(b)]. The lower threshold velocity for carbon ions, v_L^C is slightly larger than v_L^P as the charge-to-mass ratio, Z_i/A_i,

FIG. 3. (a) The electrostatic field E_x (left axis, blue line) and potential ϕ (right axis, red line) at $t = 3.0$ ps. The normalized proton n_H/n_{cr} (left axis, blue line) and carbon n_C/n_{cr} (right axis, red line) densities at (b) $t = 3.0$ ps and (c) $t = 4.0$ ps in C_2H_3Cl plasma for $a_0 = 10$. Panel (a) is shown across a narrow longitudinal range compared with panels (b) and (c).

is a factor of two smaller for C^{6+}. Furthermore, because of the smaller Z_i/A_i, the expansion velocity v_0^C driven by E_{TNSA} in the upstream region is lower than equivalent process for protons. This causes v_0^C to drop below v_L^C. This is illustrated in Fig. 2(b) which highlights how few C^{6+} ions are accelerated. Indeed, some of the energetic C^{6+} ions in Fig. 2(b) likely originate early in time from the laser interaction at the front surface of the plasma. We conclude that a negligible number of C^{6+} ions are accelerated via the CSA mechanism for $a_0 = 3.35$.

Simulations at low-intensity ($a_0 = 3.35$) generate a single-shock. At higher intensity, a key finding is the appearance of two distinct collisionless shocks. Figure 3 shows results at $a_0 = 10$, and Fig. 3(a) illustrates the longitudinal electrostatic field E_x averaged over the y-axis, and potential ϕ at $t = 3.0$ ps. Large-amplitude changes in E_x and ϕ are present at two different longitudinal positions. Large changes in the normalized proton and C^{6+} ion densities are indicated, respectively, by the dotted ($x \approx 112$ μm) and solid ($x \approx 126$ μm) vertical lines in Fig. 3(b). Figure 3(c) shows how the normalized ion populations have evolved 1 ps later at $t = 4.0$ ps. It is clear that the position of the jump in proton and C^{6+} ion densities are different.

Multiple shock structures are seen in the phase-space and velocity spectra in the first and second columns, respectively, of Fig. 4. The three sets of data are for single-component H, single-component C, and multicomponent C_2H_3Cl plasmas at $t = 4.0$ ps. The positions of the shock fronts highlighted in Figs. 4(c) and 4(e) are at the same longitudinal locations as the jumps in n_H/n_{cr} and n_C/n_{cr} identified in Fig. 3(c). A large number of protons and some of the C^{6+} ions have velocities greater than v_L^i and so CSA increases the velocity of these ions to $2V_{sh}^i - v_L^i$. In the C_2H_3Cl plasma, collisionless shocks associated with the protons and separately with the C^{6+} ions accelerate the protons and C^{6+} ions to different velocities. Figures 4(c) and 4(e) indicate that the multicomponent C_2H_3Cl plasma develops, in the expanding upstream, a broad velocity distribution within the proton and C^{6+} ion populations. This is driven by an electrostatic ion two-stream instability (EITI) that arises from the velocity differences between the proton population with $Z_i/A_i = 1$, and the heavier C^{6+} ions with $Z_i/A_i = 0.5$. We refer to this as heavy-ion EITI or HI-EITI [59]. We find that the HI-EITI decelerates some upstream protons, while it accelerates some C^{6+} ions with velocities below v_L^C to velocities that exceed this lower
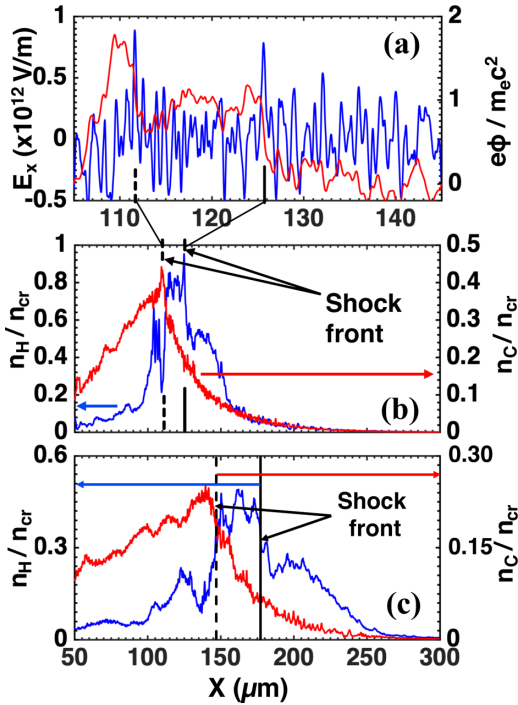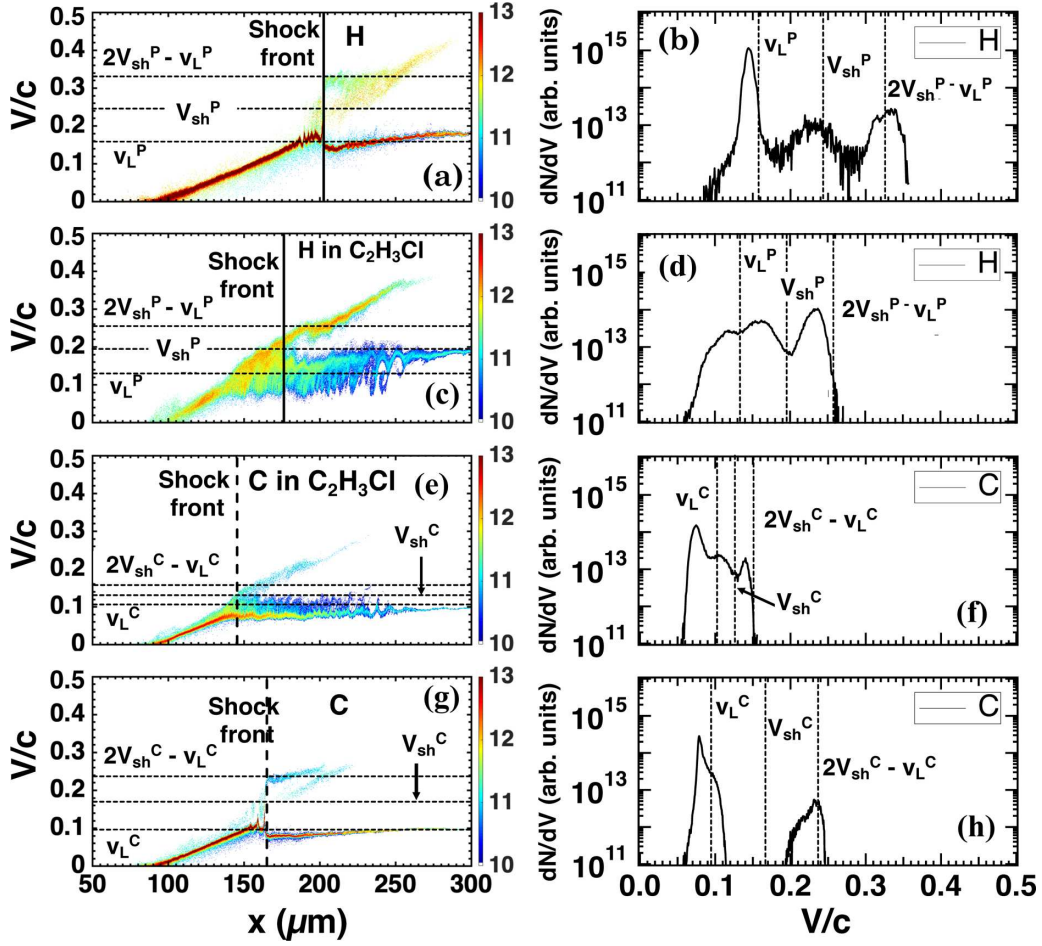
FIG. 4. The first and second columns indicate the ion phase-space and the velocity spectra respectively for $a_0 = 10$ and at $t = 4.0$ ps. The velocity spectra are taken in the upstream region immediately in front of the shock across $\Delta x = 3$ μm. (a), (b) Results for protons from a single-component H plasma. (c), (d) Results for protons from a C_2H_3Cl plasma. (e), (f) Results for C^{6+} ions from a C_2H_3Cl plasma. (g), (h) Results for C^{6+} ions in single-component C plasma. The vertical lines in phase-space in panels (a), (c), (e), and (g) identify the position of the shock front. In panels (b), (d), (f), and (h), moving left to right, the dotted lines indicate the positions of the lower threshold velocity v_L^i, shock velocity V_{sh}^i, and the maximum velocity of the reflected ions, $2V_{sh}^i - v_L^i$. The color scale shows the number of ions on a log scale.

threshold, and thereby increases the population of C^{6+} ions available for CSA [59]. Furthermore, the CSA reflected-ion population, which moves at high velocity, causes an additional EITI with the slower moving expanding plasma that forms

the upstream. We refer to this as reflected-ion EITI or RI-EITI [59]. Overall, RI-EITI accelerates the slower upstream expanding ions towards higher velocity and promotes some ions, both protons and C^{6+} ions, with velocities below v_L^i to
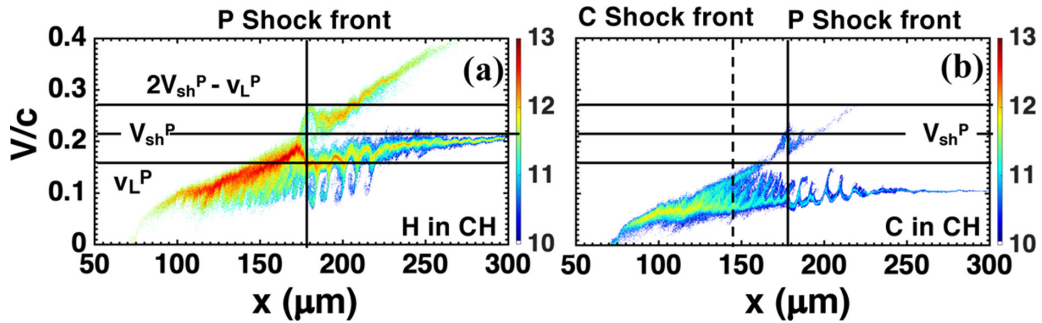

FIG. 5. The phase space for (a) protons and (b) C^{6+} ions from a CH plasma for $a_0 = 10$ and at $t = 4.0$ ps. The vertical lines identify the positions of the shock front associated with the protons (solid line) and the C^{6+} ions (dashed line). The horizontal lines indicate the positions of the lower threshold velocity v_L^P and shock velocity V_{sh}^P of protons, and the maximum velocity of the reflected protons, $2V_{sh}^P - v_L^P$. The color scale shows the number of ions in a log scale.

velocities above the lower threshold. This further increases the ion population available for CSA [59]. In a multicomponent C_2H_3Cl plasma, both RI-EITI and HI-EITI play essential roles in enabling the acceleration of C^{6+} ions.

B. Double-step shock acceleration

In the previous section, the multiple-shock (proton shock and C^{6+}-ion shock) formation is described in a multicomponent C_2H_3Cl plasma at $a_0 = 10$, and protons and C^{6+} ions are reflected and accelerated by each shock once. In this section, we illustrate C^{6+}-ion acceleration is a double-step process with reflections at each shock in a multicomponent CH plasma at $a_0 = 10$.

Figures 5 show the phase-space for protons [Fig. 5(a)] and C^{6+} ions [Fig. 5(b)] in a CH plasma at $a_0 = 10$ and $t = 4.0$ ps. We see that in this CH plasma, the high-mass C^{6+} ions are reflected and accelerated twice; first at the C^{6+} ion shock ($x \approx 143 \ \mu m$) and second at the proton shock ($x \approx 177 \ \mu m$) to the velocity $V/c = 0.23$. This is a clear observation of double-step multiple-shock acceleration of high-mass C^{6+} ions in a multicomponent plasma. This double-step shock acceleration of C^{6+} ions is clearly seen in Fig. 5 but not in a C_2H_3Cl plasma [Fig. 4]. This is caused by a slightly faster proton-shock velocity of $V_{sh}^P/c = 0.22$ in a CH plasma compared with $V_{sh}^P/c = 0.20$ in a C_2H_3Cl plasma. As a result, in a CH plasma V_{sh}^P is larger than the velocity of the pre-accelerated C^{6+} ions, which are reflected and accelerated by the C^{6+}-ion shock and likely originated from the laser interaction at the front surface of the plasma early in time. This results in the second acceleration of C^{6+} ions by the proton shock. In the case of a C_2H_3Cl plasma, V_{sh}^P is nearly equal to the velocity of the pre-accelerated C^{6+} ions, and the second acceleration of C^{6+} ions is not observed.

Furthermore, the respective deceleration and acceleration of expanding proton and C^{6+} ion populations, as a result of HI-EITI, are more apparent in a CH plasma compared with a C_2H_3Cl plasma.

C. The a_0 dependence of plasma parameters

Simulations show the formation of two collisionless shocks at $a_0 \geqslant 10$, and CSA of a significant number of C^{6+} ions in multicomponent plasmas. This is qualitatively different from simulations at $a_0 = 3.35$ which show, see in Fig. 2(b), a single shock. To understand the importance of increasing a_0, we extend our numerical investigation of CSA to $a_0 = 20$ and 33 in a C_2H_3Cl plasma. These simulations confirm the existence of two collisionless shocks and indicate that the Mach number depends on a_0.

In Fig. 6(a) we compare, at $t = 4.0$ ps, the upstream electron energy distributions for different a_0 and fit these with two-dimensional-relativistic (2D-relativistic) Maxwellian functions. The distributions at $a_0 = 10$, 20, and 33 are described by a two-temperature fit representing a bulk population and an energetic tail, while at $a_0 = 3.35$ the distribution is described by a single temperature. The bulk and tail Maxwellian components are shown for $a_0 = 33$. Figure 6(b) shows an a_0 power-law dependence for temperatures associated with the bulk and high-energy parts of the electron distributions. The fitted electron temperatures
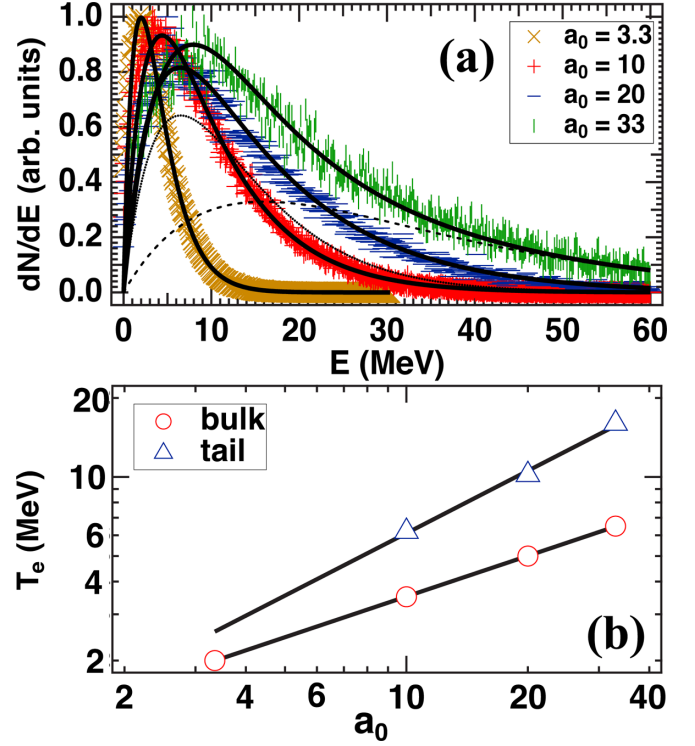

FIG. 6. (a) The electron energy distribution taken at $t = 4.0$ ps in the upstream region of the shock front for different laser intensities corresponding to $a_0 = 3.35$ (×), 10 (+), 20 (-), and 33 (|) for C_2H_3Cl. A sum of two (bulk and tail) 2D relativistic Maxwellian is used to fit to the electron energy distribution shown by the solid lines for $a_0 = 10$, 20, and 33. The bulk (dotted line) and tail (dashed line) components for $a_0 = 33$ are shown. (b) The electron temperatures as a function of a_0.

do not depend on the target material, as the laser intensity and the electron densities are not material dependent but determined by a_0 [59].

The shock velocity V_{sh}^i and the mean velocity v_m^i of the expanding ions for all values of a_0 are higher in single-component H and C plasmas, compared with a multicomponent C_2H_3Cl plasma. Furthermore, the difference between V_{sh}^i and v_m^i, $v_{df}^i = V_{sh}^i - v_m^i$, increases with a_0 as a power-law except at the highest intensity, where $a_0 = 33$, which results from significant levels ion reflection depleting or dissipating the collisionless shock [74].

Figures 7(a) and 7(b) represent the shock velocity V_{sh}^i and the mean velocity v_m^i, respectively, of the expanding protons and C^{6+} ions as a function of a_0 in a single-component H plasma, single-component C plasma, and C_2H_3Cl plasmas. The proton and C^{6+}-ion V_{sh}^i and v_m^i are always larger for the single-component H plasma and single-component C plasma compared with the multicomponent C_2H_3Cl plasma and follow the trend $V_H^P > V_{C_2H_3Cl}^P > V_C^C > V_{C_2H_3Cl}^C$ for all laser intensities. Here superscripts P and C denote protons and C^{6+} ions, respectively, with different plasmas indicated by subscripts. The ordering of velocities results from differences in the average charge-to-mass ratio $\langle Z \rangle / \langle A \rangle$, that is as V_{sh}^i and v_m^i are predominantly determined by the ion-acoustic velocity c_s^i and velocity of ions due to E_{TNSA}, respectively. Differences
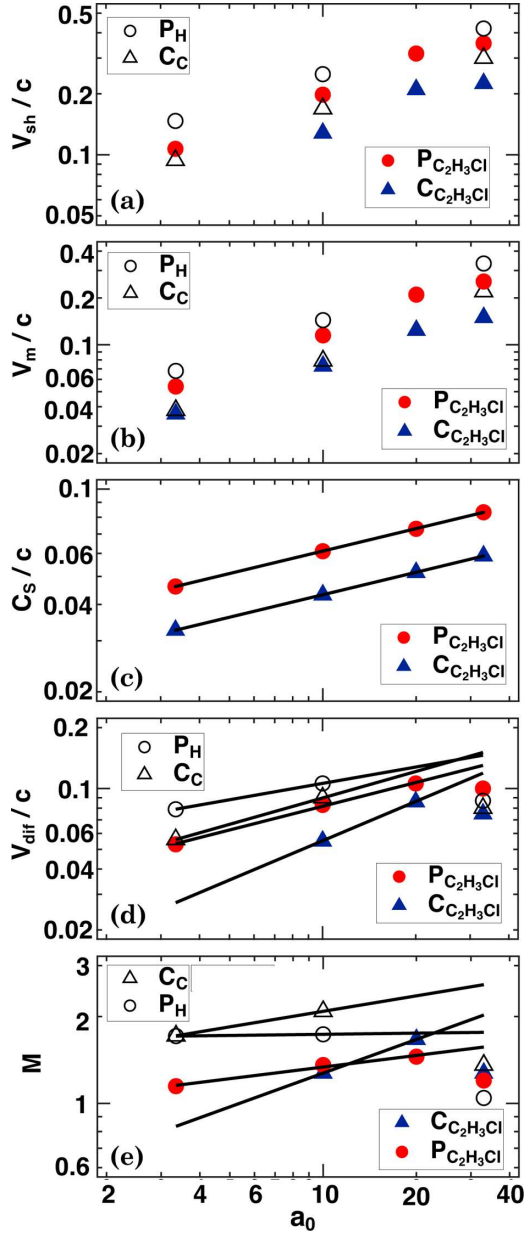
FIG. 7. The a_0 dependence of (a) shock velocities V_{sh}^i, (b) mean velocities of the expanding ions v_m^i, (c) ion-acoustic velocities c_s^i, (d) difference between the shock velocity and mean velocity of the expanding ions $v_{df}^i = V_{sh}^i - v_m^i$, and (e) the corresponding Mach number $M^i = v_{df}^i/c_s^i$ at $t = 4.0$ ps for protons in a single-component H plasma (○), C^{6+} ions in a single-component C plasma (△), and protons (●) and C^{6+} ions (▲) in a multicomponent C_2H_3Cl plasma.

in the hole-boring velocity, which depends on $\sqrt{\langle Z \rangle / \langle A \rangle}$, explains why $V_H^P > V_{C_2H_3Cl}^P$ and $V_C^C > V_{C_2H_3Cl}^C$ [59]. As a result, the shock velocity in a single-component H plasma (with $\langle Z \rangle / \langle A \rangle = 1$) is larger than that in C_2H_3Cl ($\langle Z \rangle / \langle A \rangle = 0.48$), and shock velocity for C^{6+} ion in a single-component C plasma ($\langle Z \rangle / \langle A \rangle = 0.50$) is larger than that in C_2H_3Cl.

Ion-acoustic waves are excited in proton and C^{6+} ion populations and using the bulk electron temperatures T_e to derive an ion-acoustic velocity, $c_s^i = \sqrt{(Z_i/A_i)T_e/m_p}$, we find that the associated Mach numbers, $M^i = v_{df}^i/c_s^i$, scale as a

power law in a_0. The ion-acoustic velocities for protons (c_s^P) and C^{6+} ions (c_s^C) are calculated by using the bulk temperature of the plasma. The upstream bulk temperatures in a single-component H plasma, single-component C plasma, and multicomponent C_2H_3Cl plasma are the same: as a result the c_s^i depends on the $\sqrt{\langle Z \rangle / \langle A \rangle}$. This is shown in Fig. 7(c). The c_s^i, indicated by the solid lines, scale with a_0 as a power-law. The difference between the shock velocity and mean velocity of the expanding ions, i.e., $v_{df}^i = V_{sh}^i - v_m^i$, is shown in Fig. 7(d) and increases as a power-law with a_0 except at $a_0 = 33$.

The ratio between the v_{df}^i and c_s^i yields the Mach number $M^i = v_{df}^i/c_s^i$, this is shown in Fig. 7(e). In comparison with M^P, the Mach number for protons, M^C, the Mach number for C^{6+} ions, has a strong scaling with a_0. Notice in multicomponent C_2H_3Cl, $M^C < 1$ for $a_0 = 3.35$, and no shock is associated with the C^{6+} ions. Furthermore, M^P in a single-component H plasma decreases with a_0; this occurs as v_m^P scales faster with a_0 than V_{sh}^P, causing a slow scaling of v_{df}^P compared with c_s^P as a_0 increases.

D. Shock dissipation

For $a_0 = 33$ shock dissipation, driven by ion reflection, becomes more pronounced. This reduces the shock velocity [74]. Evidence for this is seen in Fig. 7(d) of v_{df}^i and in Fig. 7(e) of M^i which illustrate a power-law trend for $a_0 = 3.35$, 10, and 20 up to the end of the simulations at $t = 4.0$ ps. Simulations at $a_0 = 33$ show significant shock dissipation from $t \approx 2.5$ ps. For $a_0 = 3.35$, 10, and 20, shock velocities increase exponentially with time until $t = 4.0$ ps, in contrast, for $a_0 = 33$, the shock velocity increases to $t < 2.5$ ps then dissipates, which results in low Mach numbers at $a_0 = 33$ for single- and multicomponent plasmas [74].

The temporal variation of shock positions (X_{sh}) in a single-component H plasma and a multicomponent C_2H_3Cl plasma for $a_0 = 3.35$ are shown in Fig. 8(a). The derivative dX_{sh}/dt gives the shock velocity V_{sh}. Since there is an exponential drop in the density at the rear-side of the target, V_{sh} increases exponentially as a function of time for all target materials. For $a_0 = 3.35$ [see Fig. 8(a)], 10, and 20, X_{sh} and V_{sh} rise exponentially with time. Comparing this to Fig. 8(b), we see that at $a_0 = 33$ the temporal evolution of X_{sh} and V_{sh} for protons and C^{6+} ions in a multicomponent C_2H_3Cl plasma is slower. Indeed, the time dependencies of X_{sh} and V_{sh} are best represented by third- and second-order polynomials, respectively. This slower temporal evolution results from enhanced ion reflection at the shock which increases shock dissipation [74].

E. The a_0 dependence of ion acceleration

Figures 9(a) and 9(b) show how the energy E and the number of reflected ions at the peak of the energy distribution dN/dE depend on a_0. In the C_2H_3Cl plasma there are no C^{6+}-associated shocks at $a_0 = 3.35$ as $M^C < 1$. The energies of the reflected ions are always larger in single-component H or C plasma when compared with multicomponent C_2H_3Cl plasma [Fig. 9(a)]. This is a feature of smaller V_{sh}^i and ampli-
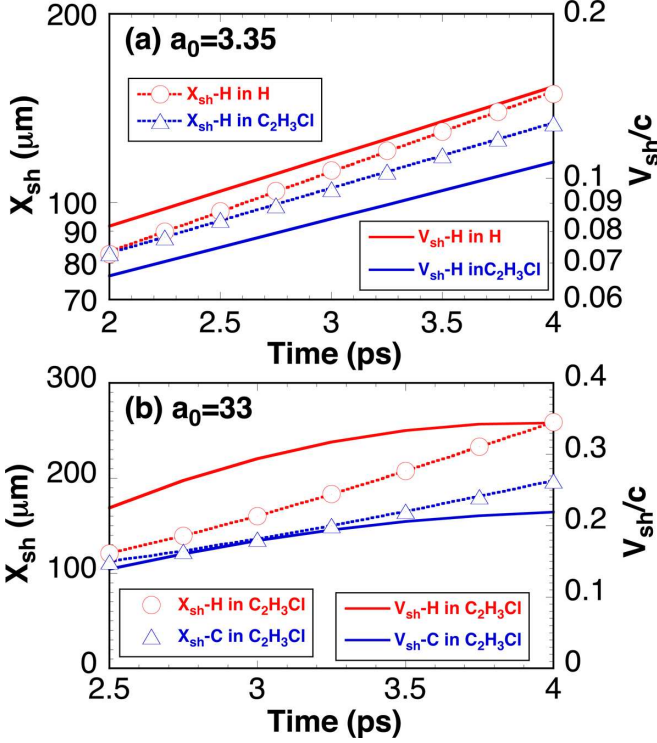
FIG. 8. (a) The temporal evolution of shock positions X_{sh} and shock velocities V_{sh} for protons in a single-component H plasma (shown in red) and a multicomponent C_2H_3Cl plasma (shown in blue) for $a_0 = 3.35$. X_{sh} data are shown as open circles (a single-component H plasma: $\bigcirc$) and open triangles (a multicomponent C_2H_3Cl plasma: $\triangle$). The derivative of X_{sh} with respect to time gives V_{sh}. X_{sh} (dotted lines) and V_{sh} (solid lines) rise exponentially with time. (b) The temporal evolution of X_{sh} and V_{sh} for protons (shown in red) and C^{6+} ions (shown in blue) in a multicomponent C_2H_3Cl plasma for $a_0 = 33$. X_{sh} data are shown as open circles (protons: $\bigcirc$) and open triangles (C^{6+} ions: $\triangle$). The time dependencies of X_{sh} and V_{sh} are best represented by a third-order (dotted lines) and second-order (solid lines) polynomials, respectively.

tude of ϕ in the multicomponent C_2H_3Cl compared with the single-component H or C plasma as shown in Fig. 4.

Figures 10(a) and 10(b) show the spatial profile of electrostatic potentials ϕ in a multicomponent C_2H_3Cl plasma and a single-component H plasma, respectively, at $t = 2.5$ (blue curve) and 4.0 ps (red curve) for $a_0 = 3.35$. The vertical lines indicate the position of the shock fronts. These highlight that ϕ is smaller in a multicomponent C_2H_3Cl plasma compared with a single-component H plasma. The smaller ϕ is a result of a lower $\langle Z \rangle / \langle A \rangle$ plasma. In a single-component H plasma, the gradient $d\phi/dx$ is large. This potential jump is associated with the shock and is necessary for ion acceleration. It is produced by a charge separation between electrons and ions. This feature is not observed in the multicomponent C_2H_3Cl plasma because the charge separation between electrons and ions is smeared out over a larger volume by the heavier C and Cl ions, as a result the amplitude and gradient associated with ϕ are smaller.

Our PIC results indicate that V_{sh} is smaller at lower $\langle Z \rangle / \langle A \rangle$, this is explained by recognizing that the hole-boring
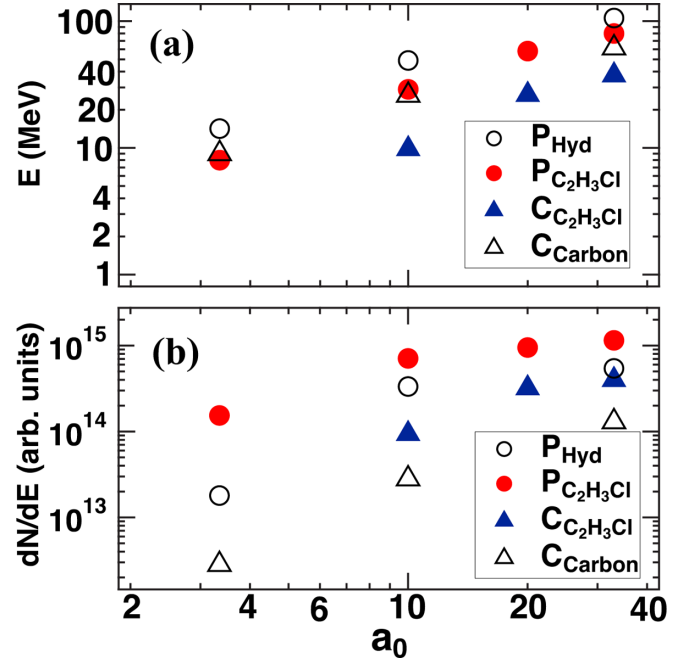

FIG. 9. The a_0 dependence of (a) energy E per nucleon and (b) the number dN/dE at E of reflected protons and C^{6+} ions at the peak of the energy distribution at $t = 4.0$ ps for protons in single-component H ($\bigcirc$), C^{6+} ions in single-component C ($\triangle$), and protons ($\bullet$) and C^{6+} ions ($\blacktriangle$) in C_2H_3Cl plasmas.

velocity [75]

$$V_{HB} = c \sqrt{a_0^2 \frac{\langle Z \rangle}{\langle A \rangle} \frac{m_e}{m_p} \frac{n_{cr}}{n_e}} \tag{2}$$

determines the velocity of the piston driving the collisionless shock. Given that a_0 and n_e are same for all target materials, V_{HB} has relative dependence on only $\sqrt{\langle Z \rangle / \langle A \rangle}$, maximizing V_{sh} when $\langle Z \rangle / \langle A \rangle$ is largest, i.e., for a single-component H plasma.

For the multicomponent C_2H_3Cl plasma at $a_0 > 3.35$ the flux of the reflected protons and C^{6+} ions is higher [see Fig. 9(b)]. It is important to note that more protons are accelerated in multicomponent plasma as v_L^P is lower in comparison to the single-component H plasma. For C^{6+} ion acceleration, HI-EITI, which is present only in a multicomponent plasma, broadens the velocity distribution of the expanding C^{6+} ions towards higher velocity. This results in more C^{6+} ions being available for CSA in comparison with single-component C plasmas.

These results confirm our earlier observation [59] that only proton collisionless shocks were observed in multicomponent plasmas at $a_0 = 3.35$. In this work Mach numbers $M = 1.6$–1.7 were calculated with a critical Mach number needed for the proton reflection and CSA. These values were derived using ion-acoustic velocities based on a $\langle Z \rangle / \langle A \rangle$, where $\langle Z \rangle$ and $\langle A \rangle$ are the respective averages of $\langle Z_i \rangle$ and $\langle A_i \rangle$ across all ion species in a plasma. Here, we use ion-specific ion-acoustic velocities to describe the two collisionless shocks. For protons c_s^P determines the Mach number M^P of a proton collisionless shock, and ions satisfying the reflection condition given by
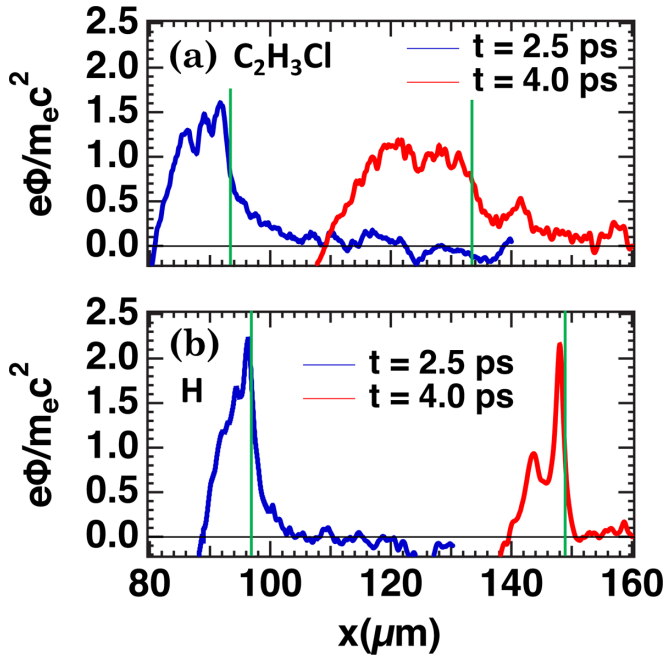
FIG. 10. The spatial profile of electrostatic potentials in (a) a multicomponent C_2H_3Cl plasma and (b) a single-component hydrogen plasma at $t = 2.5$ (blue curves) and 4.0 ps (red curves) for $a_0 = 3.35$. The vertical lines indicate the position of the shock fronts.

Eq. (1) are accelerated even when the Mach number is less than M_{cr} defined in Ref. [59].

IV. SUMMARY

Two-dimensional PIC simulations are used to investigate the evolution of electrostatic collisionless shocks and CSA

of protons and heavy ions in multicomponent plasmas. The interaction of a high-intensity p-polarized laser with C_2H_3Cl and CH plasmas leads to the formation of the two shock fronts in proton and C^{6+}-ion populations. Both shocks have different amplitudes of the shock potential and propagate with different velocities. The electron temperature, shock velocities, and Mach numbers for shocks associated with proton (M^P) and C^{6+} ions (M^C) scale as a power-laws with the normalized laser intensity a_0. In the multicomponent C_2H_3Cl plasma, M^C scales faster with a_0 compared with M^P. At $a_0 = 3.35$, as $M^C < 1$, a C^{6+} ion-shock does not form. On increasing a_0, shock formation with CSA of protons and C^{6+} ions occurs at different location and velocities. Double-step shock acceleration is investigated in a CH plasma, in which the pre-accelerated C^{6+} ions are further accelerated at the proton-shock. A broadening upwards of the C^{6+} ion velocity distribution, as a result of a HI-EITI, is important and increases the number of C^{6+} ions accelerated. For $a_0 = 33$ shock dissipation, driven by ion reflection, becomes more pronounced. This results in the reduction of the shock velocity. Moreover, modern ultra-intense, picosecond duration lasers enable the laboratory study of the formation and modification of collisionless shocks as ions are accelerated in multicomponent plasmas. These topics are important to space physics, astrophysics, and plasma physics.

[1] R. Sagdeev and V. Shapiro, JETP Lett. **17**, 279 (1973).
[2] A. R. Bell, Mon. Not. R. Astron. Soc. **182**, 147 (1978).
[3] R. D. Blandford and J. P. Ostriker, Astrophys. J. **221**, L29 (1978).
[4] C. S. Wu, J. Geophys. Res. **89**, 8857 (1984).
[5] L. Ball and D. B. Melrose, Publ. Astron. Soc. Aust. **18**, 361 (2001).
[6] M. Hoshino, Prog. Theor. Phys. Suppl. **143**, 149 (2001).
[7] Y. Sakawa, T. Morita, Y. Kuramitsu, and H. Takabe, Adv. Phys.: X **1**, 425 (2016).
[8] K. Sauer, Geophys. Res. Lett. **23**, 3643 (1996).
[9] H. Shimazu, J. Geophys. Res. **106**, 8333 (2001).
[10] C. Mazelle, D. Winterhalter, and K. Sauer, Space Sci. Rev. **111**, 115 (2004).
[11] C. Bertucci, F. Duru, N. Edberg, M. Fraenz, C. Martinecz, K. Szego, and O. Vaisberg, Space Sci. Rev. **162**, 113 (2011).
[12] R. Jarvinen, D. A. Brain, R. Modolo, A. Fedorov, and M. Holmström, J. Geophys. Res. **123**, 1678 (2018).
[13] M. Yamauchi, Y. Futaana, A. Fedorov, R. A. Frahm, E. Dubinin, R. Lundin, J. A. Sauvaud, J. D. Winningham, S. Barabash, and M. Holmström, Earth, Planets Space **64**, 61 (2012).

[14] D. A. Gurnett, W. S. Kurth, L. F. Burlaga, and N. F. Ness, Science **341**, 1489 (2013).
[15] N. Borisov and M. Fraenz, Phys. Plasmas **23**, 122109 (2016).
[16] C. Bertucci, C. Mazelle, M. H. Acuña, C. T. Russell, and J. A. Slavin, J. Geophys. Res. **110**, A01209 (2005).
[17] J. S. Warren, J. P. Hughes, C. Badenes, P. Ghavamian, C. F. McKee, D. Moffett, P. P. Plucinsky, C. Rakowski, E. Reynoso, and P. Slane, Astrophys. J. **634**, 376 (2005).
[18] D. Caprioli, D. T. Yi, and A. Spitkovsky, Phys. Rev. Lett. **119**, 171101 (2017).
[19] B. D. Metzger, Liv. Rev. Relativ. **23**, 1 (2020).
[20] H. Yamaguchi, K. A. Eriksen, C. Badenes, J. P. Hughes, N. S. Brickhouse, A. R. Foster, D. J. Patnaude, R. Petre, P. O. Slane, and R. K. Smith, Astrophys. J. **780**, 136 (2014).
[21] I. J. Cohen, S. J. Schwartz, K. A. Goodrich, N. Ahmadi, R. E. Ergun, S. A. Fuselier, M. I. Desai, E. R. Christian, D. J. McComas, G. P. Zank, J. R. Shuster, S. K. Vines, B. H. Mauk, R. B. Decker, B. J. Anderson, J. H. Westlake, O. Le Contel, H. Breuillard, B. L. Giles, R. B. Torbert, and J. L. Burch, J. Geophys. Res. **124**, 3961 (2019).

[22] J. M. Broll, S. A. Fuselier, K. J. Trattner, S. J. Schwartz, J. L. Burch, B. L. Giles, and B. J. Anderson, Geophys. Res. Lett. **45**, 49 (2018).

[23] D. B. Schaeffer, W. Fox, J. Matteucci, K. V. Lezhnin, A. Bhattacharjee, and K. Germaschewski, Phys. Plasmas **27**, 042901 (2020).

[24] T. Byvank, S. J. Langendorf, C. Thoma, and S. C. Hsu, Phys. Plasmas **27**, 042302 (2020).

[25] P. W. Rambo and J. Denavit, Phys. Plasmas **1**, 4050 (1994).

[26] C. Bellei, H. Rinderknecht, A. Zylstra, M. Rosenberg, H. Sio, C. K. Li, R. Petrasso, S. C. Wilks, and P. A. Amendt, Phys. Plasmas **21**, 056310 (2014).

[27] H. Sio, J. A. Frenje, A. Le, S. Atzeni, T. J. T. Kwan, M. Gatu Johnson, G. Kagan, C. Stoeckl, C. K. Li, C. E. Parker, C. J. Forrest, V. Glebov, N. V. Kabadi, A. Bose, H. G. Rinderknecht, P. Amendt, D. T. Casey, R. Mancini, W. T. Taitano, B. Keenan, A. N. Simakov, L. Chacón, S. P. Regan, T. C. Sangster, E. M. Campbell, F. H. Seguin, and R. D. Petrasso, Phys. Rev. Lett. **122**, 035001 (2019).

[28] H. G. Rinderknecht, H. S. Park, J. S. Ross, P. A. Amendt, S. C. Wilks, J. Katz, N. M. Hoffman, G. Kagan, E. L. Vold, B. D. Keenan, A. N. Simakov, and L. Chacón, Phys. Plasmas **25**, 056312 (2018).

[29] C. N. Danson, C. Haefner, J. Bromage, and T. Butcher, High Power Laser Sci. Eng. **7**, e54 (2019).

[30] H. Daido, M. Nishiuchi, and A. S. Pirozhkov, Rep. Prog. Phys. **75**, 056401 (2012).

[31] A. Macchi, M. Borghesi, and M. Passoni, Rev. Mod. Phys. **85**, 751 (2013).

[32] S. V. Bulanov, J. J. Wilkens, T. Z. Esirkepov, G. Korn, G. Kraft, S. D. Kraft, M. Molls, and V. Khoroshkov, Phys. Usp. **57**, 1149 (2014).

[33] C. K. Li, F. H. Séguin, J. A. Frenje, J. R. Rygg, R. D. Petrasso, R. P. J. Town, P. A. Amendt, S. P. Hatchett, O. L. Landen, A. J. Mackinnon, P. K. Patel, V. A. Smalyuk, T. C. Sangster, and J. P. Knauer, Phys. Rev. Lett. **97**, 135003 (2006).

[34] M. Roth, T. E. Cowan, M. H. Key, S. P. Hatchett, C. Brown, W. Fountain, J. Johnson, D. M. Pennington, R. A. Snavely, S. C. Wilks, K. Yasuike, H. Ruhl, P. Pegoraro, S. V. Bulanov, E. M. Campbell, M. D. Perry, and H. Powell, Phys. Rev. Lett. **86**, 436 (2001).

[35] R. A. Snavely, M. H. Key, S. P. Hatchett, T. E. Cowan, M. Roth, T. W. Phillips, M. A. Stoyer, E. A. Henry, T. C. Sangster, M. S. Singh, S. C. Wilks, A. MacKinnon, A. Offenberger, D. M. Pennington, K. Yasuike, A. B. Langdon, B. F. Lasinski, J. Johnson, M. D. Perry, and E. M. Campbell, Phys. Rev. Lett. **85**, 2945 (2000).

[36] S. C. Wilks, A. B. Langdon, T. E. Cowan, M. Roth, M. Singh, S. Hatchett, M. H. Key, D. Pennington, A. MacKinnon, and R. A. Snavely, Phys. Plasmas **8**, 542 (2001).

[37] F. Wagner, O. Deppert, C. Brabetz, P. Fiala, A. Kleinschmidt, P. Poth, V. A. Schanz, A. Tebartz, B. Zielbauer, M. Roth, T. Stöhlker, and V. Bagnoud, Phys. Rev. Lett. **116**, 205002 (2016).

[38] G. G. Scott, D. C. Carroll, S. Astbury, R. J. Clarke, C. Hernandez-Gomez, M. King, A. Alejo, I. Y. Arteaga, R. J. Dance, A. Higginson, S. Hook, G. Liao, H. Liu, S. R. Mirfayzi, D. R. Rusby, M. P. Selwood, C. Spindloe, M. K. Tolley, F. Wagner, E. Zemaityte, M. Borghesi, S. Kar, Y. Li, M. Roth, P. McKenna, and D. Neely, Phys. Rev. Lett. **120**, 204801 (2018).

[39] T. Esirkepov, M. Borghesi, S. V. Bulanov, G. Mourou, and T. Tajima, Phys. Rev. Lett. **92**, 175003 (2004).

[40] A. Henig, S. Steinke, M. Schnürer, T. Sokollik, R. Hörlein, D. Kiefer, D. Jung, J. Schreiber, B. M. Hegelich, X. Q. Yan, J. Meyer-ter-Vehn, T. Tajima, P. V. Nickles, W. Sandner, and D. Habs, Phys. Rev. Lett. **103**, 245003 (2009).

[41] A. Macchi, S. Veghini, and F. Pegoraro, Phys. Rev. Lett. **103**, 085003 (2009).

[42] I. J. Kim, K. H. Pae, I. W. Choi, C.-L. Lee, H. T. Kim, H. Singhal, J. H. Sung, S. K. Lee, H. W. Lee, P. V. Nickles, T. M. Jeong, C. M. Kim, and C. H. Nam, Phys. Plasmas **23**, 070701 (2016).

[43] A. Higginson, R. J. Gray, M. King, R. J. Dance, S. D. R. Williamson, N. M. H. Butler, R. Wilson, R. Capdessus, C. Armstrong, J. S. Green, S. J. Hawkes, P. Martin, W. Q. Wei, S. R. Mirfayzi, X. H. Yuan, S. Kar, M. Borghesi, R. J. Clarke, D. Neely, and P. McKenna, Nat. Commun. **9**, 724 (2018).

[44] L. Yin, B. J. Albright, B. M. Hegelich, and J. C. Fernández, Laser Part. Beams **24**, 291 (2006).

[45] A. Henig, D. Kiefer, K. Markey, D. C. Gautier, K. A. Flippo, S. Letzring, R. P. Johnson, T. Shimada, L. Yin, B. J. Albright, K. J. Bowers, J. C. Fernández, S. G. Rykovanov, H.-C. Wu, M. Zepf, D. Jung, V. K. Liechtenstein, J. Schreiber, D. Habs, and B. M. Hegelich, Phys. Rev. Lett. **103**, 045002 (2009).

[46] D. J. Stark, L. Yin, and B. J. Albright, Phys. Plasmas **26**, 123101 (2019).

[47] J. Denavit, Phys. Rev. Lett. **69**, 3052 (1992).

[48] L. O. Silva, M. Marti, J. R. Davies, R. A. Fonseca, C. Ren, F. Tsung, and W. B. Mori, Phys. Rev. Lett. **92**, 015002 (2004).

[49] F. Fiuza, A. Stockem, E. Boella, R. A. Fonseca, L. O. Silva, D. Haberberger, S. Tochitsky, C. Gong, W. B. Mori, and C. Joshi, Phys. Rev. Lett. **109**, 215001 (2012).

[50] D. Haberberger, S. Tochitsky, F. Fiuza, C. Gong, R. A. Fonseca, L. O. Silva, W. B. Mori, and C. Joshi, Nat. Phys. **8**, 95 (2011).

[51] O. Tresca, N. P. Dover, N. Cook, C. Maharjan, M. N. Polyanskiy, Z. Najmudin, P. Shkolnikov, and I. Pogorelsky, Phys. Rev. Lett. **115**, 094802 (2015).

[52] H. Zhang, B. F. Shen, W. P. Wang, Y. Xu, Y. Q. Liu, X. Y. Liang, Y. X. Leng, R. X. Li, X. Q. Yan, J. E. Chen, and Z. Z. Xu, Phys. Plasmas **22**, 013113 (2015).

[53] H. Zhang, B. F. Shen, W. P. Wang, S. H. Zhai, S. S. Li, X. M. Lu, J. F. Li, R. J. Xu, X. L. Wang, X. Y. Liang, Y. X. Leng, R. X. Li, and Z. Z. Xu, Phys. Rev. Lett. **119**, 164801 (2017).

[54] P. Antici, E. Boella, S. N. Chen, D. S. Andrews, M. Barberio, J. Böker, F. Cardelli, J. L. Feugeas, M. Glesser, P. Nicolaï, L. Romagnani, M. Scisciò, M. Starodubtsev, O. Willi, J. C. Kieffer, V. Tikhonchuk, H. Pépin, L. O. Silva, E. D. Humières, and J. Fuchs, Sci. Rep. **7**, 16463 (2017).

[55] S. N. Chen, M. Vranic, T. Gangolf, E. Boella, P. Antici, M. Bailly-Grandvaux, P. Loiseau, H. Pépin, G. Revet, J. J. Santos, A. M. Schroer, M. Starodubtsev, O. Willi, L. O. Silva, E. d'Humières, and J. Fuchs, Sci. Rep. **7**, 13505 (2017).

[56] A. Pak, S. Kerr, N. Lemos, A. Link, P. Patel, F. Albert, L. Divol, B. B. Pollock, D. Haberberger, D. Froula, M. Gauthier, S. H. Glenzer, A. Longman, L. Manzoor, R. Fedosejevs, S. Tochitsky, C. Joshi, and F. Fiuza, Phys. Rev. Accel. Beams **21**, 103401 (2018).

[57] J. Polz, A. P. Robinson, A. Kalinin, G. A. Becker, R. A. Fraga, M. Hellwing, M. Hornung, S. Keppler, A. Kessler, D. Klöpfel, H. Liebetrau, F. Schorcht, J. Hein, M. Zepf, R. E. Grisenti, and M. C. Kaluza, Sci. Rep. **9**, 16534 (2019).

[58] M. Ota, A. Morace, R. Kumar, S. Kambayashi, S. Egashira, M. Kanasaki, Y. Fukuda, and Y. Sakawa, High Energy Density Phys. **33**, 100697 (2019).

[59] R. Kumar, Y. Sakawa, L. N. K. Döhl, N. Woolsey, and A. Morace, Phys. Rev. Accel. Beams **22**, 043401 (2019).

[60] D. Forslund and C. Shonk, Phys. Rev. Lett. **25**, 281 (1970).

[61] D. W. Forslund, R. L. Morse, and C. W. Nielson, Phys. Rev. Lett. **27**, 1424 (1971).

[62] A. Balogh and R. A. Treumann, *Physics of Collisionless Shocks: Space Plasma Shock Waves* (Springer Science & Business Media, New York, 2013)

[63] L. O. Drury, Rep. Prog. Phys. **46**, 973 (1983).

[64] F. C. Jones, Space Sci. Rev. **58**, 259 (1991).

[65] Y. Ohira and F. Takahara, Astrophys. J. **688**, 320 (2008).

[66] R. A. Treumann, Astron. Astrophys. Rev. **17**, 409 (2009).

[67] H. Madanian, S. J. Schwartz, J. S. Halekas, and L. B. Wilson, Geophys. Res. Lett. **47**, e2020GL088309 (2020).

[68] S. D. Bale and F. S. Mozer, Phys. Rev. Lett. **98**, 205001 (2007).

[69] S. D. Bale, P. J. Kellogg, F. S. Mozer, T. S. Horbury, and H. Reme, Phys. Rev. Lett. **94**, 215002 (2005).

[70] X. Zhang, B. Shen, L. Ji, F. Wang, Z. Jin, X. Li, M. Wen, and J. R. Cary, Phys. Rev. ST Accel. Beams **12**, 021301 (2009).

[71] T. D. Arber, K. Bennett, C. S. Brady, A. Lawrence-Douglas, M. G. Ramsay, N. J. Sircombe, P. Gillies, R. G. Evans, H. Schmitz, A. R. Bell, and C. P. Ridgers, Plasma Phys. Control. Fusion **57**, 113001 (2015).

[72] T. Grismayer and P. Mora, Phys. Plasmas **13**, 032103 (2006).

[73] D. A. Tidman and N. A. Krall, *Shock Waves in Collisionless Plasmas* (Wiley-Interscience, New York, 1971).

[74] T. V. Liseykina, G. I. Dudnikova, V. A. Vshivkov, and M. A. Malkov, J. Plasma Phys. **81**, 495810507 (2015).

[75] A. P. Robinson, P. Gibbon, M. Zepf, S. Kar, R. G. Evans, and C. Bellei, Plasma Phys. Control. Fusion **51**, 024004 (2009).